**THE ROYAL
SOCIETY**

Propagation through nonlinear time-dependent bubble clouds and the estimation of bubble populations from measured acoustic characteristics

BY T. G. LEIGHTON, S. D. MEERS AND P. R. WHITE

Institute of Sound and Vibration Research, University of Southampton, Highfield, Southampton SO17 1BJ, UK (tgl@soton.ac.uk)

For several decades the propagation characteristics of acoustic pulses (attenuation and sound speed) have been inverted in attempts to measure the size distributions of gas bubbles in liquids. While this has biomedical and industrial applications, most notably it has been attempted in the ocean for defence and environmental purposes, where the bubbles are predominantly generated by breaking waves. Such inversions have required assumptions, and the state-of-the-art technique still assumes that the bubbles undergo linear, steady-state monochromatic pulsations in the free field, without interacting. The measurements always violate, to a greater or lesser extent, these assumptions. The errors incurred by the use of such assumptions have been difficult to quantify, but are expected to be most severe underneath breakers in the surf zone, where the void fraction is greatest. Very few measurements have been made in this important region of the ocean. This paper provides a method by which attenuation can be predicted through clouds of bubbles which need not be homogeneous, nor restricted to linear steady-state monochromatic pulsations. To allow inversion of measured surf zone attenuations to estimate bubble populations with current computational facilities, this model is simplified such that the bubble cloud is assumed to be homogeneous and the bubbles oscillating in steady state (although still nonlinearly). The uses of the new methods for assessing the errors introduced in using state-of-the-art inversions are discussed, as are their implications for oceanographic and industrial nonlinear bubble counters, for biomedical contrast agents, and for sonar target detection in the surf zone.

Keywords: acoustic propagation; bubble; oceanic bubble size distribution;
acoustic cross-section; echo-contrast agents; sonar target detection

1. Introduction

The ability to determine the sizes and numbers of gas bubbles in a population has biomedical, defence, environmental and industrial applications (Leighton 1994*a*). If the acoustic propagation is linear, it may be modelled using a complex representation, and the introduction of a bubble population into the liquid is assumed to result

in a modification of the complex wavenumber. Measurement of the changes in acoustic attenuation and phase speed caused by the addition of bubbles is at first sight simple enough, and has been frequently attempted over the last 50 years (Medwin & Clay 1998). The bubble population is then estimated by inverting these measured propagation characteristics using some model. Given the long history of application of this technique, it is therefore surprising that the assumptions inherent in the models are still extensive. All measurements violate one or more or these assumptions. The state-of-the-art inversion (Commander & McDonald 1991; Melville *et al.* 1997; Dumbrell 1997; Duraiswami *et al.* 1998; Terrill & Melville 1998; Terrill *et al.* 2001) is based on a theory (Commander & Prosperetti 1989) which assumes that the bubbles are undergoing steady-state monochromatic linear pulsations in the free field without interacting.

In general, the greater the range of bubble radii present in the population, and the greater the void fraction (the proportion of a given volume of bubbly water that comprises free gas), the greater the extent to which the assumptions of the inversion are violated when the measurement is made. This is not simply because of the non-interaction condition, but also because the greater reverberation and attenuation which result from higher void fractions will tend to promote the use of shorter insonifying pulses of higher amplitude. The problem is that, provided the inversion converges to a plausible solution, the temptation is to accept that solution without examining its correctness. Prior to this paper, such examinations could only be attempted by comparing the solution with the result of an independent (e.g. optical) measurement. Such comparisons are rarely done, and are of limited use because of differences in the sampling, and the limitations of bubble radius range and resolution (Stokes & Deane 1999), that are inherent to the different techniques. With intense surf zone breakers, they become impractical. However, without such testing, it is not even possible to put limits of confidence on the result of the state-of-the-art inversion, unless there is a technique which is not so constrained by assumptions.

This study presents such an advance, based on methods of predicting attenuation in inhomogeneous bubble clouds without the assumptions of linearity, monochromaticity and steady-state bubble pulsations (the 'forward problem'). This technique is of use when high driving pressures are incident on the bubble population being measured, causing a nonlinear response, or when the excitation is sufficiently short that not all bubbles are oscillating in steady-state. Incorporating the assumptions of steady-state and cloud homogeneity to allow for tractable computing times, bubble populations are estimated from the measured propagation (the 'inverse' problem) in the surf zone in November 2001. The results are processed using both the state-of-the-art technique and the new approach.

The ocean represents probably the most common of the challenging environments where inversions are made to estimate bubble populations. The population estimates so obtained have been used for a variety of processes, including studies of the fluxes of mass, energy and momentum between the atmosphere and the ocean (Thorpe 1982; Thorpe *et al.* 1992; Farmer *et al.* 1993), and for enhancement of the operation of sonar in the surf zone (Meers *et al.* 2001). The populations so encountered can be sufficiently polydisperse, and have a high enough void fraction, for it to be reasonable to question the effects of violating the key assumptions. (While it is possible to find populations with higher void fractions, for example, in the food industry, an advance in theory is probably a prerequisite before bubble size distributions are
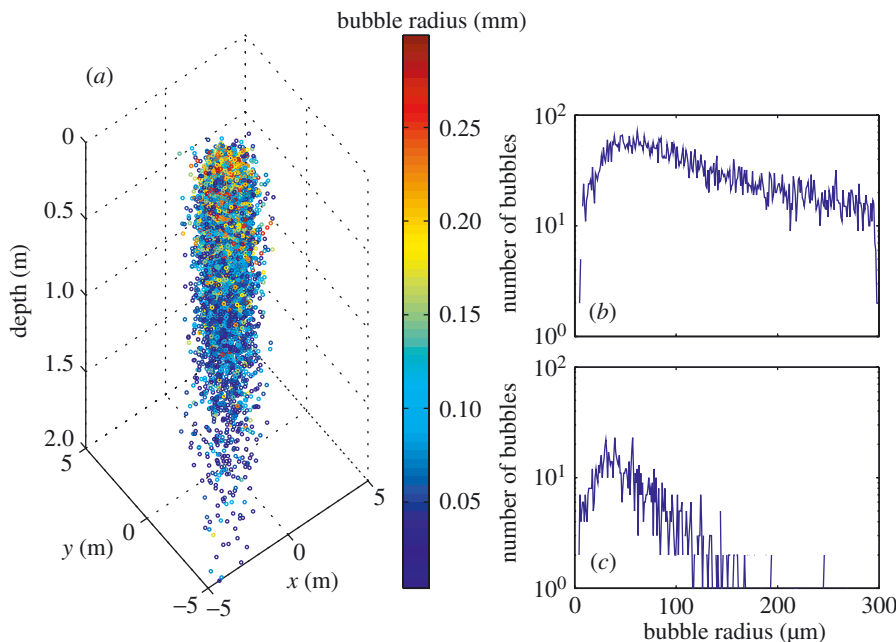
Figure 1. A single frame from an animation by M. D. Simpson and T. G. Leighton (available at http://www.isvr.soton.ac.uk/fdag/UAUA/research.html). The air–sea interface is flat and at depth 0 m; the sea bed is flat and at depth 2 m. A bubble population is injected into a three-dimensional section of ocean measuring $2\,\text{m} \times 10\,\text{m} \times 10\,\text{m}$. This 'entrainment' population is based on measurements of the passive noise from breaking waves, and the bubbles are introduced at the origin. The population then evolves under the influence of buoyancy, turbulence, surface tension and hydrostatic pressure, and gas flux occurs as, for example, the bubbles dissolve (Thorpe 1982; Phelps & Leighton 1998). (*a*) The bubble cloud 30 s after injection. The bubble size distribution is colour coded, and it is, for example, clear that, while turbulence has dispersed the cloud spatially, both buoyancy and hydrostatic effects result in the tendency for small bubbles (blue) to appear at depth, with the larger (yellow/orange/red) bubbles tending to occur only close to the surface. Leighton (2001) investigated the accuracy of such models by comparing the predicted bubble population as a function of depth with the measurements of active acoustic techniques, such as those described in this paper. The two frames on the right show the bubble size distribution (number of bubbles per cubic metre per micrometre radius increment, as described in the text): (*b*) volume-integrated result from depth 0 to 1 m; (*c*) the volume-integrated result from depths of 1 m to the bottom (2 m). The peak in the population at a bubble radius *ca.* 30–50 μm is more apparent in the bottom plot. This is because at these greater depths the influence of hydrostatic pressure and dissolution (which tend to cause bubbles to shrink the deeper they go) and buoyancy (which tends to allow only the smaller bubbles to travel to depth) will be stronger than the effect of turbulence (which tends to homogenize the cloud). Each of the 64 000 bubbles in the simulation represents *ca.* 10^4 bubbles in nature because of computational limitations (hence the difference in magnitude on the vertical axes in figures 1 and 9). (First presented by Leighton (2001).)

realistically measured in these.) Bubbles in the ocean are generated through a variety of processes, including biological activity, methane seeps, rainfall, etc. However, the most important near-surface entrainment mechanism is wave breaking. This is not only because of the number of bubbles involved, but also because of the ability of

waves to entrain large bubbles which greatly affect the stability of the inversion (see below). The bubble populations generated in the surf zone breakers are especially problematic in this respect, and most of the at-sea bubble size distributions have been measured in deeper waters (Melville *et al.* 1997; Terrill & Melville 1998; Farmer 2001; Didenkulov *et al.* 2001). Those trials taken in the 'surf zone' tend to deploy sensors in the relatively quiet transition region (Svendsen *et al.* 1978), $O(100)$ m offshore. Even those taken in shallow water (depths less than 2 m) tend to occur on sandy beaches with slopes of gentler than 1 in 70 (Leighton *et al.* 1996; Phelps *et al.* 1997; Deane 1997; Terrill *et al.* 2001; Farmer *et al.* 2001; Dahl 2001), so that the sensors tend to be *ca.* 100 m offshore and the breaker activity is dispersed over a wide zone. Very few (Meers *et al.* 2001; Leighton *et al.* 2001; Leighton 2001) have been taken on shingle beach slopes steeper than 1 in 9, where all the dissipation from breakers is confined to an intense region within *ca.* 20 m of the shoreline. It is in this most difficult region that the measurements in this paper are taken.

This paper discusses the most commonly used active acoustic technique, where the attenuation of an acoustic signal between two points is related to the number of bubbles per cubic metre per unit bubble-size bin (i.e. $n(R_0)$, where $n(R_0)\,\mathrm{d}R_0$ is the number of bubbles per cubic metre having radii between R_0 and $R_0 + \mathrm{d}R_0$, and where the radius bin width $\mathrm{d}R_0$ is usually taken to be 1 μm). There are alternative techniques, and these are usually listed with respect to the differences in hardware or signals employed (Leighton 1994*b*; Nyborg 2002). What is rarely considered is that these techniques can be measuring different bubble populations: a particularly important point, as in recent years the trend has been to compare the results obtained using various techniques in an attempt to cross-validate them. While the 'measurement volume' in the bubble density considered in this paper is an output of the plane-wave assumption (see §2), for combination-frequency systems it comes directly from the well-defined volume of liquid formed by the cross-over of the various transducer beam patterns (which are of course frequency dependent) (Phelps *et al.* 1997; Sutin *et al.* 1998; Phelps & Leighton 1998; Didenkulov *et al.* 2001). The bubble-mediated signals generated by the active acoustic techniques, such as those described above, in principle include information from all the bubbles in the measurement volume, because they are all driven to pulsate by an incident sound field. Whether of course these signals are interpreted as a measure of all the bubbles present is a function of the accuracy of the inversion algorithm, to be discussed shortly. In contrast, passive acoustic techniques monitor the net sound field which results from the impulsive excitation of bubbles. In practice this usually consists of monitoring the overlapping emissions of bubbles excited upon entrainment in babbling brooks and waterfalls (Leighton & Walton 1987), under breaking waves (Updegraff & Anderson 1989; Medwin & Beaky 1989; Deane & Stokes 2002), rainfall or 'dripping taps' (Pumphrey *et al.* 1989): to first order each bubble produces an exponentially decaying sinusoid at a natural frequency which is roughly inversely proportional to its radius (Minnaert 1933). However, this population of 'ringing' bubbles is a subset of the total bubble population that an active acoustic technique would measure, a fact which should be recognized when the two are compared. Indeed, it is a difference which can be exploited, for example, in order to determine from their difference how the population entrained under a breaking waves evolves into the steady-state ocean population as a result of dissolution, bubble fragmentation and coalescence, buoyancy, depth changes, etc. (figure 1). Even amongst optical techniques, the population
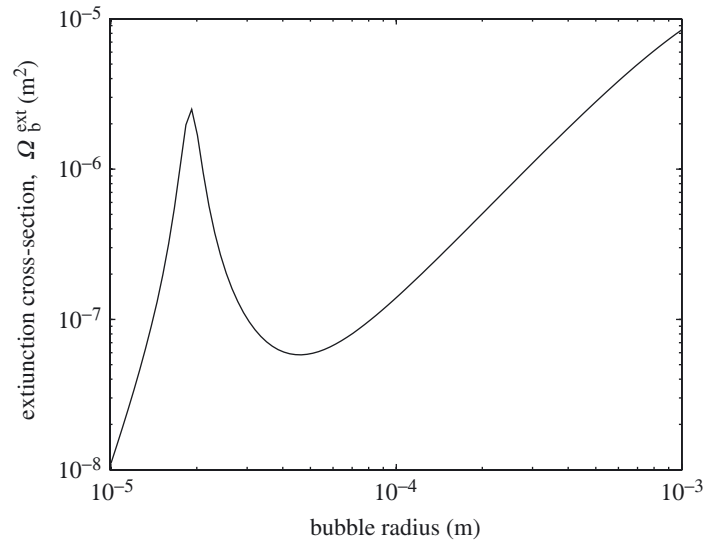
Figure 2. Extinction cross-section for a fixed frequency of 165 kHz as a function of bubble radius. Note that there is only a local maximum at resonance.

is sampled. In photography the sample volume can be inferred from the depth of field blurring (Geissler & Jahne 1997) or by illuminating only a known volume (Stokes & Deane 1999), while, if a count is made of those bubbles which have risen under buoyancy to settle under a glass plate (Kolovayev 1976), the volume of seawater sampled for the larger bubbles (which have the greater buoyant rise speed) of course exceeds that sampled for the smaller bubbles. While it is possible optically to count bubbles having radii from 10 μm (Su *et al.* 1994) up to more than 1 mm (Stokes & Deane 1999), this cannot be done for a constant 'field of view'.

The popularity of the state-of-the-art method of inverting measured propagation along an array to estimate bubble populations probably stems from several sources, one of which is the ability to encompass a wide range of bubble radii across a single 'field of view' (§ 2). Also, in an environment where every cubic metre of wave water which impacts on the rig has a mass of a tonne, its ruggedness is probably an overwhelming factor. Another might be its frequent ability to generate a result. The new version described here uses the same rugged hardware (although the durability and deployment requirements for trials taken on steep shingle beaches, as in this paper, may exceed those of deployments made further offshore on shallow, sandy beaches, the historically more popular site). The fundamental advance of the current study over the state-of-the-art method is in the models used to interpret the data. In both versions, each gas bubble is driven to pulsate by an incident sound field, and acts as a resonant system: the stiffness comes primarily from the gas component, and the inertia from the surrounding liquid (Leighton 1994a). Prior to the 1960s there were doubts as to whether micro-bubbles existed in the sea at all. That they exist in great numbers was demonstrated by Medwin (1977). A peak in the $n(R_0)$ distribution was found by Farmer & Vagle (1989), who, for a depth of 0.1 m below the sea surface in water 140 m deep, estimated numbers in excess of 10^5 m^{-3} in the micrometre-radius bin centred on 20 μm. The earliest inversions assumed that only resonant bubbles contributed to the observed changes in sound speed and attenuation. Although this

rather extreme assumption is still applied in some inversions today, most accept the guidance that in general the presence of off-resonant bubbles needs to be considered (Commander & Moritz 1989). The importance of large bubbles, for example, can be shown in figure 2 where the extinction cross-section at a fixed frequency is plotted as a function of bubble radius. For a single bubble, the extinction cross-section ($\Omega_{\mathrm{b}}^{\mathrm{ext}}$) is defined as the ratio of the power lost through acoustic absorption and scatter, to the intensity of the incident acoustic wave (which is assumed to be planar). The cross-section has dimensions of area and can be thought of as representing, for a single bubble, the 'target area' it presents to the beam. As can be seen from figure 2, although there is a local maximum at resonance (20 μm), large bubbles can contribute as significantly as resonant bubbles, not by pulsating at large amplitude but simply by virtue of their size. This illustrates how the nature of the extinction cross-section leads to ill conditioning in the inversion problem (Commander & McDonald 1991). This point is expanded upon in § 3.

The cross-section discussed above is indeed still found at the heart of the state-of-the-art inversions (equation (2.16) will ingeminate that this description of attenuation is based upon the effect on a solution to the linearized plane-wave equation of an appropriate summation of the extinction cross-sections of the bubbles in the population). The pioneering state-of-the-art propagation model for the inversion was provided by Commander & Prosperetti (1989) (and has been cited over 100 times since), with various inversion routes tried over the following decade and more (Commander & McDonald 1991; Duraiswami *et al.* 1998). As such, the state-of-the-art method has the same limitations as the cross-section, which follow from the assumptions listed above. In addition, practical considerations usually mean that the bubbles are insonified by a pulse of finite duration, which adds conceptual difficulties to the state-of-the-art technique. For example, even if a time-dependent cross-section can be defined during the ring-up to steady state (Clarke & Leighton 2000), the extinction cross-section clearly becomes undefined once the driving field has ceased but the damped bubble continues to undergo decaying pulsations. If the cross-section concept is abandoned, the power loss during the ring-down period can still be calculated, by combining a nonlinear description of the bubble-wall time history with a linear monochromatic damping constant (Clarke & Leighton 2000). If the latter is evaluated at a frequency corresponding to a period twice the zero-crossing interval of the radius, the damping constant becomes appropriately time-dependent. In practice, during ring-down, the simplification that the bubble oscillates at its natural frequency can be made (see figure 10). Fundamentally, however, the damping would still be based on a linear model, even though the time history with which it is combined can encompass nonlinearities. In § 2 we use the first law of thermodynamics to produce a method capable of calculating nonlinear and time-dependent losses at all times during insonification.

2. Theory

The insightful review of the propagation issues by Commander & Prosperetti (1989) is recommended to readers (as are the key texts by van Wijngaarden (1968) and Caflisch *et al.* (1985)). By linearizing the problem, they predict the effects on acoustic phase speed and attenuation that the addition of bubbles to a previously bubble-free liquid will have, through consideration of the complex wavenumber of plane

waves. Such an approach is not possible for the nonlinear problem, where complex representation is inappropriate. Assume throughout that each bubble radius is much smaller than the acoustic wavelength. A cloud of bubbly water, having volume V_c and bulk modulus B_c, is made up of a volume V_w of bubble-free water (having sound speed c_w and bulk modulus B_w) and a volume V_g of free gas (having sound speed c_g and bulk modulus B_g) distributed in a population of bubbles, and hence

$$V_c = V_w + V_g. \tag{2.1}$$

Mass conservation is simply expressed by multiplication of the volumes with the respective densities (of the cloud, ρ_c, bubble-free water, ρ_w, and gas, ρ_g), i.e.

$$\rho_c V_c = \rho_w V_w + \rho_g V_g. \tag{2.2}$$

Under the assumption that each of the three media conserve mass separately, the differential of equation (2.2) with respect to the applied pressure P is, of course, zero. In an infinite body of either water or gas that contains *no dissipation*, sound speeds (c_w and c_g, respectively) may be defined according to

$$c_\varepsilon^2 = \frac{B_\varepsilon}{\rho_\varepsilon} = \left[\frac{\partial P(\rho, S)}{\partial \rho}\right]_\varepsilon, \quad \varepsilon = \text{w}, \text{g}, \tag{2.3}$$

where S is the entropy and the subscript ε can refer to application to water (w) or gas (g). Similarly, differentiation of equation (2.1) with respect to the applied pressure gives, with equation (2.3), the relationship between the bulk moduli:

$$\frac{1}{B_c} = \frac{V_w}{V_c}\frac{1}{B_w} + \frac{V_g}{V_c}\frac{1}{B_g}. \tag{2.4}$$

Let us define a function ξ_c (which is not an inherent property of the bubble cloud in the thermodynamic sense), equal to the root of the ratio of the bulk modulus of the bubbly cloud to its density, which with equation (2.4) gives

$$\xi_c = \sqrt{\frac{B_c}{\rho_c}} = \sqrt{\left(\frac{V_c}{\rho_w V_w + \rho_g V_g}\right)\left(\frac{V_w}{V_c B_w} + \frac{V_g}{V_c B_g}\right)^{-1}} \approx c_w \left(1 + \frac{B_w V_g(t)}{V_c B_g(t)}\right)^{-1/2}, \tag{2.5}$$

where the final approximation is valid under low-void-fraction conditions. Specifically, it is assumed that the density and volume of the cloud are approximately equal to those of its bubble-free water component. If the bubbly cloud were not dissipative, then this would equal the sound speed in the cloud, but (as will be shown) such an identity is not rigorous in lossy bubble clouds.

Evaluation of equation (2.5) requires calculation of the bulk modulus of the gas, as it is distributed through a (presumably) numerous population of bubbles pulsating with a broad range of amplitudes, phases, frequency content, damping and start times. The inhomogeneous bubbly water must be divided into volume elements which are sufficiently small to ensure that all the bubbles in that element are subjected to the same pressure change $\text{d}P(t)$ simultaneously. This would allow calculation of a value for ξ_c for each volume element, since from equation (2.3) the bulk modulus B_{gl} of the gas within the lth element is related to the volume changes $\text{d}V_i$ of the I bubbles in that volume element,

$$\frac{1}{B_{gl}} = -\frac{1}{V_{gl}}\sum_{i=1}^{I}\frac{\text{d}V_i}{\text{d}P_l}, \tag{2.6}$$

where P_l denotes the pressure in the lth volume element. Consider one such volume element V_{cl} of a cloud which has total volume

$$V_c = \sum_{l=1}^{L} V_{cl}. \tag{2.7}$$

Substituting equation (2.6) into equation (2.5) gives ξ_{cl}, the time history of ξ_c within the volume element V_{cl},

$$\xi_{cl} \approx c_w \left(1 - \frac{\rho_w c_w^2}{V_{cl}} \sum_{i=1}^{I} \frac{\mathrm{d}V_i}{\mathrm{d}P_l} \right)^{-1/2}. \tag{2.8}$$

To understand the meaning of this quantity, consider that, if the system were linear, monodisperse and lossless, $\mathrm{d}V_i/\mathrm{d}P_l$ would be a constant throughout the oscillatory cycle: in pressure–volume space, as one progressed throughout the oscillatory cycle one would move back and forth along a locus of points mapping out a straight line. The constant gradient of that line could be related to the sound speed in the cloud through equation (2.8), which would equal the constant ξ_{cl}. If the system were nonlinear and lossless, $\mathrm{d}V_i/\mathrm{d}P_l$ would vary through the cycle, and the single line mapped out by the locus of points in pressure–volume space would not be straight. In this case the sound speed would vary through the oscillatory cycle, and could again be identified with ξ_{cl} through equation (2.8). This could then be related to a sound speed for nonlinear propagation. If, however, dissipation occurs, the locus of points in the pressure–volume plane would, during a single oscillatory cycle, map out a finite area. In such circumstances ξ_{cl} cannot strictly be identified with any sound speed. If dissipation is very small, then one might identify a characteristic value of $\mathrm{d}V_i/\mathrm{d}P_l$ which is not much different from the true value for most of the acoustic cycle; for the linearized case, this is in effect what Commander & Prosperetti do. This will be discussed further in relation to figure 4.

To evaluate equation (2.8), the bubble population of the volume element is classified into j discrete bins according to bubble size. Every individual bubble in the jth bin is replaced by another bubble which oscillates with radius $R_j(t)$ and volume $V_j(t)$ (about equilibrium values of R_{0_j} and V_{0_j}), such that the total number of bubbles N_j and total volume of gas $N_j V_j(t)$ in the bin remain unchanged by the replacement. If the bin-width increment is sufficiently small (1 μm is normally chosen), the time history of every bubble in that bin should closely resemble $V_j(t) = V(R_{0_j}, t)$ (the sensitivity being greatest around resonance). Hence, the total volume of gas in the lth volume element of bubbly water is

$$V_{gl}(t) = \sum_{j=1}^{J} N_j(R_{0_j}, t) V_j(t) = V_{cl} \sum_{j=1}^{J} n_j(R_{0_j}, t) V_j(t). \tag{2.9}$$

Here $n_j(R_{0_j}, t) = N_j(R_{0_j}, t)/V_{cl}$ is the number of bubbles per unit volume of bubbly water within the jth bin. It will vary more slowly than the acoustically driven pulsation $V_j(t)$, and so the approximation is made that it is stationary over the duration of the measurement. This in practice can be in the range 0.001–1 s; smaller volume elements and more dynamic oceans would sensibly suggest finer time resolu-

tion. Expressing equation (2.8) in terms of this bin scheme gives

$$\xi_{cl} \approx c_{\mathrm{w}} \left(1 - \rho_{\mathrm{w}} c_{\mathrm{w}}^2 \sum_{j=1}^{J} n_j(R_{0_j}) \frac{\mathrm{d}V_j(t)}{\mathrm{d}P_l(t)} \right)^{-1/2}. \tag{2.10}$$

Crucially, equation (2.10) provides a generic framework into which any bubble dynamics model may be inserted (giving $\mathrm{d}V_j(t)/\mathrm{d}P_l(t)$ appropriate to bubbles in water, tubes, sediments, etc., as the chosen model dictates). Equation (2.10) contains low-void-fraction limitations identical to those discussed by Commander & Prosperetti (1989). However, so far no assumptions of small amplitude, steady-state, monochromatic or linear bubble pulsations have been included, nor have the bubbles and their wall motions been assumed to be spherically symmetric. If these assumptions are introduced, the state-of-the-art formulation is recovered, as follows. If the oscillations are spherically symmetric and of small amplitude, then

$$\frac{\mathrm{d}V}{V_0} = \left(1 + \left(\frac{\mathrm{d}R}{R_0} \right) \right)^3 - 1 = 3 \left(\frac{\mathrm{d}R}{R_0} \right) + 3 \left(\frac{\mathrm{d}R}{R_0} \right)^2 + \left(\frac{\mathrm{d}R}{R_0} \right)^3. \tag{2.11}$$

Truncating after the first term in the expansion is one of the linear assumptions that may be included, and with this

$$\frac{\mathrm{d}V}{\mathrm{d}P} = 4\pi R_0^2 \left(\frac{\mathrm{d}R}{\mathrm{d}P} \right).$$

Substituting this limitation into equation (2.10), then expanding the square root binomially and re-expressing the bubble population as a continuous integral, gives

$$\frac{c_{\mathrm{w}}^2}{\xi_{\mathrm{c}}^2} \approx 1 - \rho_{\mathrm{w}} c_{\mathrm{w}}^2 \int_0^{\infty} n(R_0) \frac{\mathrm{d}V}{\mathrm{d}P} \, \mathrm{d}R_0$$

$$\approx 1 - 4\pi \rho_{\mathrm{w}} c_{\mathrm{w}}^2 \int_0^{\infty} n(R_0) R_0^2 \frac{\mathrm{d}R}{\mathrm{d}P} \, \mathrm{d}R_0, \tag{2.12}$$

where the subscript l has been dropped because the cloud in the state-of-the-art inversion has always been considered to be homogeneous.

If it is further assumed that the linear bubble pulsations are the steady-state, monochromatic response to a constant-amplitude (P_{A}) monochromatic driving field of the form $P(t) = P_{\mathrm{A}} \mathrm{e}^{\mathrm{i}\omega t}$, then (Leighton 1994a)

$$\frac{\mathrm{d}R}{\mathrm{d}P} = \frac{-1}{R_0 \rho_{\mathrm{w}}((\omega_0^2 - \omega^2) + \mathrm{i}2\beta_{\mathrm{tot}}\omega)}, \tag{2.13}$$

where $\mathrm{i} = \sqrt{-1}$, ω_0 is the undamped natural frequency of the bubble and β_{tot} is a damping constant having dimensions of time^{-1}, derived assuming monochromatic conditions, that accounts for the bubble damping by viscous, thermal and acoustic radiation mechanisms (and others, potentially). Equation (2.13) provides the state-of-the-art model with the required constant value for $\mathrm{d}V/\mathrm{d}P$ for each bubble driven under given monochromatic conditions, allowing equation (2.10) to generate a phase speed, a feature which is not strictly possible with finite dissipation, as discussed earlier.

Substitution of (2.13) into (2.12), and multiplication by the square of the angular frequency ω gives the complex wavenumber k_{c} within the bubbly mixture, as derived

by Commander & Prosperetti (1989, eqn 35), and used in the state-of-the-art inversions discussed in §1:

$$k_{\rm c}^2 \approx \left(\frac{\omega}{c_{\rm w}}\right)^2 + 4\pi\omega^2 \int_0^\infty \frac{R_0 n(R_0)}{(\omega_0^2 - \omega^2) + {\rm i}2\beta_{\rm tot}\omega}\,{\rm d}R_0. \tag{2.14}$$

If a plane harmonic acoustic wave

$$P(x,t) \propto {\rm e}^{{\rm i}(\omega t - k_{\rm c}x)} = {\rm e}^{{\rm i}(\omega t - \Lambda x)}{\rm e}^{-x\chi/2} \tag{2.15}$$

were propagating at phase speed ω/Λ along the x-axis through a bubble cloud with wavenumber $k_{\rm c} = \Lambda - \frac{1}{2}{\rm i}\chi$ described by equation (2.14), the plane-wave intensity-attenuation coefficient χ can be expressed in terms of a population-weighted integration of the extinction cross-sections $\Omega_{\rm b}^{\rm ext}$ (see figure 2) of the individual bubbles (Leighton 1994a), giving a Fredholm integral equation of the first kind,

$$\chi \approx 8\pi c_{\rm w} \int_0^\infty \frac{\omega^2 \beta_{\rm tot}}{(\omega_0^2 - \omega^2)^2 + 4\beta_{\rm tot}^2\omega^2} R_0 n(R_0)\,{\rm d}R_0$$

$$= \int_0^\infty \Omega_{\rm b}^{\rm ext}(\omega, R_0)n(R_0)\,{\rm d}R_0, \tag{2.16}$$

such that the attenuation coefficient in terms of $\rm dB\,m^{-1}$ is numerically equal to $10\chi\log_{10}{\rm e}$ in the linear formulation. In order to calculate the attenuation from a bubble population which is characterized by representative bubble counts at a few discrete sizes, as discussed earlier, it is useful to discretize equation (2.16):

$$\boldsymbol{\chi} = \boldsymbol{K}\boldsymbol{n}, \tag{2.17}$$

where the vector representing the attenuation at discrete frequencies $\boldsymbol{\chi}$ is calculated from the vector $\boldsymbol{n}$, which gives the representative bubble count at a finite number of discrete bubble radii. This calculation requires evaluation of the operator matrix $\boldsymbol{K}$, the elements of which may be constructed after the manner of equation (2.16), using a simple finite-element method in which linear B splines provide the element shape functions

$$K_{qj} = \int_0^\infty \Omega_{\rm b}^{\rm ext}(\omega_q, R_{0_j})B_j(R_{0_j})\,{\rm d}R_0, \tag{2.18}$$

where the suffices q and j refer to the driving frequency and bubble radius respectively, and where $B_j(R_{0_j})$ is the jth linear B spline which represents the continuous bubble distribution as a linear combination of spline basis functions (Commander & McDonald 1991). If equation (2.17) represents the forward problem, then equation (2.18) illustrates how the extinction cross-section is at the heart of the state-of-the-art expression of this problem.

Two features of the propagation through a bubbly cloud make it strictly not possible to follow a similar route with equation (2.10) to estimate bubble populations. First, it is of course mathematically possible to produce complex entities from the real values for ξ_{cl} generated by equation (2.10) (using, for example, the Hilbert transform (figure 3)). However, $\rm Im(\xi_{cl})$ cannot be used to calculate the attenuation, because in nonlinear systems energy is transferred between frequencies, a fact that the complex sound speed model fails to take into account. Second, the values of ξ_{cl} derived from equation (2.10) cannot be equated to a sound speed, and $(\rm Re(\xi_{cl}) - c_{\rm w})$
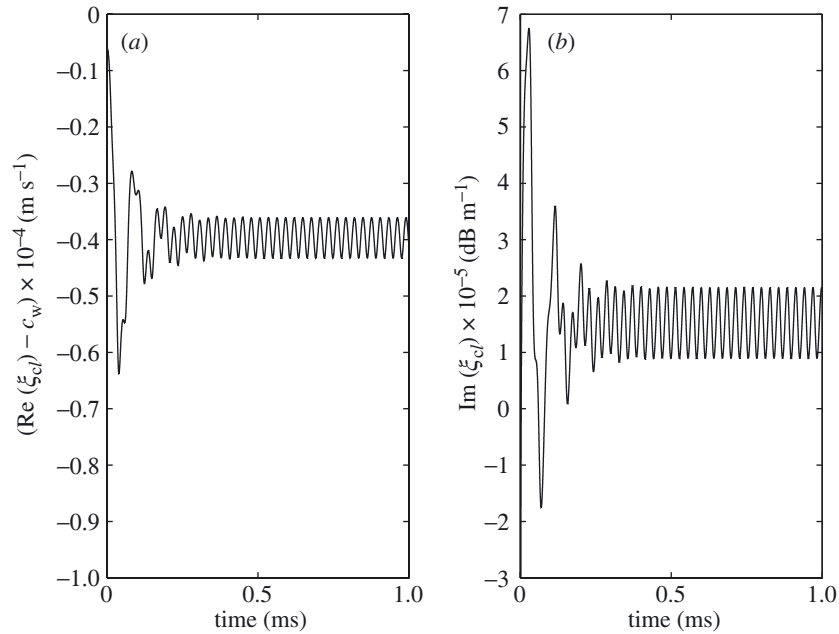
Figure 3. (a) $(\mathrm{Re}(\xi_{cl}) - c_\mathrm{w})$ and (b) $\mathrm{Im}(\xi_{cl})$, based respectively on the real and imaginary parts of equation (2.10) as constructed through use of a Hilbert transform for a single 71 μm radius bubble insonified by a 35.1 kHz semi-infinite pulse starting at $t = 0$ with an amplitude of 7.95 kPa. There is transient period lasting *ca.* 200 μs caused by the impulse response of the bubble before a steady-state oscillation is achieved.

cannot strictly be identified with the phase speed anomaly. This is because, as discussed earlier, finite dissipation means that the locus of points in the pressure–volume plane map out a finite area over the oscillatory cycle. However, it is this very feature which provides the solution by which the measured propagation characteristics can be inverted to obtain the size distribution of bubbles that are behaving nonlinearly.

Consider a plot of gas volume against applied pressure for a single bubble subjected to a semi-infinite driving pulse. The locus consists of a single point until the onset of insonification, at which it performs orbits until reaching steady-state, after which it repeatedly maps out a given orbit. Assume the gas is perfect. Its internal energy U is a state function, such that, whenever an orbit crosses its previous path, at both moments represented by the intersection the value of U is the same. More specifically, consider that

$$\mathrm{d}U = \text{đ}Q + \text{đ}W = \text{đ}Q - P\,\mathrm{d}V, \tag{2.19}$$

where the notation indicates that both the incremental heat supplied to the bubble ($\text{đ}Q$) and the work done on the bubble ($\text{đ}W$) are not exact differentials, while $\mathrm{d}U$ is.

Because the plot uses the applied acoustic pressure $P(t)$, the area mapped out by any loop represents the energy subtracted from the acoustic wave by the bubble in the time interval corresponding to the perimeter of the loop. This is because the bubble dynamics equation (such as the Keller–Miksis with thermal losses used here; see below) may be interpreted simply as a statement of the equality between that pressure difference (Δp) which is uniform across the entire bubble wall and a summation of other terms. These terms relate to the pressure within the gas and
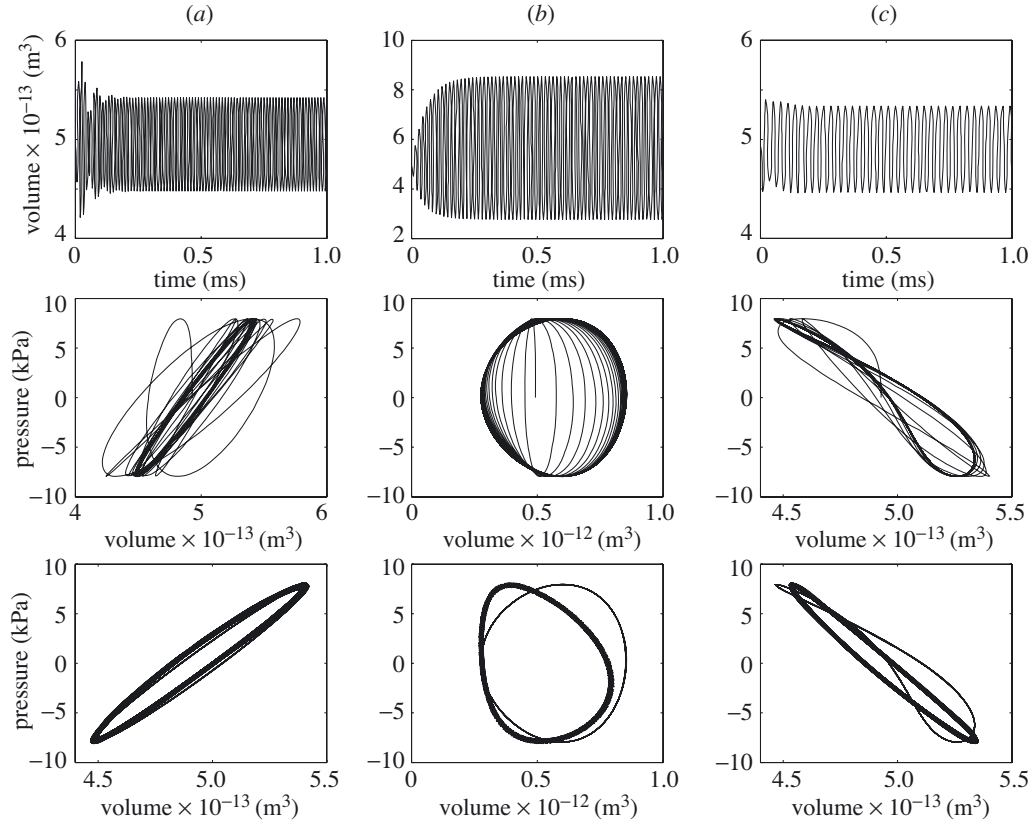
Figure 4. Bubble responses for a 49 μm radius bubble insonified by a semi-infinite pulse starting at $t = 0$ with an amplitude of 7.95 kPa at (a) 84.2 kHz, (b) 65.7 kHz and (c) 31.5 kHz. The top graph in each case shows the volume time history calculated using the Keller–Miksis equation (with damping after Prosperetti *et al.* (1988)). The middle graph in each case shows the corresponding pressure–volume curve. The darker area in each *P–V* curve shows the steady-state regime, where the successive loci overlap each other. Nonlinear components will cause crossovers in a loop (as in figure 4c, where a second harmonic arises from driving the bubble close to half resonance frequency), such that the integration of equation (2.22) causes the areas of the clockwise loops to be subtracted from those of the anticlockwise. The bottom row superimposes the steady-state loops of the middle row (thin line) with the corresponding linear solution using the steady-state formulation of Commander & Prosperetti (thick line).

vapour inside the bubble (p_i), surface tension pressures (p_σ), and the dynamic terms resulting from the motion of the liquid required when the bubble wall is displaced (Leighton 1994a), which we shall call p_{dyn}:

$$\Delta p = p_i - p_{dyn} - p_\sigma. \tag{2.20}$$

The energy subtracted from the sound field by the pulsating bubble in each circuit of a loop is given by

$$E_{loop} = - \oint p_i \, dV + \oint p_{dyn} \, dV + \oint p_\sigma \, dV \tag{2.21}$$

(noting that the details of the chemistry of the bubble wall may make the final integral non-zero). However, Δp equals the spatial average over the bubble wall of the blocked pressure $\langle p_{\mathrm{blocked}} \rangle$, which in the long-wavelength limit equals the applied acoustic pressure $P(t)$ that would be present at the bubble centre were the bubble not present. Substituting equation (2.20) into (2.21) therefore shows that the area mapped out by a loop in the pressure–volume plane is the energy subtracted from the acoustic wave in the time interval corresponding to that loop:

$$E_{\mathrm{loop}} = - \oint \Delta p \, \mathrm{d}V = - \oint \langle p_{\mathrm{blocked}} \rangle \, \mathrm{d}V \approx - \oint P \, \mathrm{d}V, \quad kR \ll 1. \qquad (2.22)$$

Therefore, the rate at which the acoustic field does work on the bubble can be found by integrating the area in the pressure–volume plane enclosed by the loops formed by the intersections described above, and dividing the energy so obtained by the time interval taken to map out that loop. In this way, the rate at which the bubble subtracts energy from the driving acoustic field can be calculated as a function of time, for example, during bubble ring-up; and while steady state is strictly only achieved as $t \to \infty$, loops approximating it can readily be identified (figure 4, middle row). Of particular interest is the bottom row of figure 4, which superimposes the steady-state nonlinear loops of the middle row (thin line) with the corresponding linear solution using the formulation of Commander & Prosperetti (which is of course steady-state; thick line). At frequencies much greater than or less than resonance (not shown), both models predict loci indistinguishable from straight lines (dissipation and nonlinearities being negligible at such extremes). The gradients of these lines have opposite signs, in keeping with standard knowledge of the sound speed for a monochromatic bubble population above and below resonance. In such cases a sound speed can be readily calculated from equations (2.8) or (2.10). Closer to resonance, increasing dissipation imparts finite areas to the loops, and the sound speed must be inferred from the 'spine' of the loop. While in some cases the nonlinear model would impart a similar spine to its loop as would that of Commander & Prosperetti (figure 4*a*), closer to resonance, identification of the optimum spine becomes more difficult (figure 4*b*; note that the conditions for resonance in the nonlinear and linear models are slightly different). The increasing dissipation and indeterminate gradient of the spine may lead to inaccuracies, and indeed Commander & Prosperetti note that 'In the presence of resonance effects, the accuracy of the model is severely impaired'. In figure 4*c*, the nonlinear model displays a second harmonic (which is of course not apparent in the linear result). The 'spine' of this double-loop would be curved, and its identification would allow calculation of nonlinear propagation through bubble clouds, waveform distortion, parametric signal generation, etc.

In this paper we will proceed, however, by using the time-dependent rate of loss of energy from the acoustic wave which nonlinear bubble oscillation engenders, as illustrated in figure 4 (the middle row). There are many routes by which the attenuation of the acoustic wave could be calculated. To follow most simply from the theory presented earlier, the power loss calculated in any time interval could be divided by the intensity of the driving sound field to generate a time-dependent nonlinear acoustic extinction cross-section. This in turn can be used in equation (2.18) to generate time-dependent, nonlinear elements for the $\boldsymbol{K}$ matrix. The method can be used to examine the evolution of the extinction cross-sections of each bubble as a function of the frequency, amplitude and pulsing characteristics

of the driving field, and similarly to follow the evolution during ring-up of the corresponding K_{qj} elements (as will be done to obtain the attenuations in figure 12.) The limits of linearity can be examined, for example, by determining under what conditions E_{loop} in the steady state departs from a linear dependence on incident intensity (e.g. for the semi-infinite driving field of amplitude P_{A} discussed earlier, nonlinearity is diagnosed by the degree to which $E_{\mathrm{loop}}/P_{\mathrm{A}}^2$ is not constant as P_{A} increases).

It is clear that evaluation of ξ_{cl} via equation (2.10) for a volume element of bubbly liquid requires calculation of $\mathrm{d}V/\mathrm{d}P$ over the relevant time period, for one bubble per size bin (these being the bubbles having equilibrium radii R_{0_j}). Similarly, calculation of the attenuation requires maps resembling figure 4 for each bubble radius, insonification frequency and amplitude considered. Clearly, the resulting values can only be as accurate as the numerical model which is used to calculate the time histories. In the small-amplitude monochromatic limit it is relatively simple to incorporate thermal, viscous and radiation losses through damping coefficients (Eller 1970; Prosperetti 1974). However, when conditions are not monochromatic (e.g. during the transient period prior to steady state for bubbles driven off-resonance; during nonlinear pulsations; or if the bubbles are driven by a non-monochromatic sound field (Didenkulov *et al.* 2001; Phelps *et al.* 1997)), then, while most nonlinear bubble dynamics models include viscous losses with relative ease, thermal and radiation damping require careful consideration. The popular Rayleigh–Plesset model includes only viscous losses, and attempts to include thermal and radiation losses through artificial 'thermal' and 'acoustic' viscosities (Prosperetti 1974) add no further physics beyond that present in the monochromatic damping coefficients. (With a polytropic gas law and the use of such an artificial viscosity to model radiation damping, Kumar & Brennen (1991, 1993) used the Rayleigh–Plesset equation to predict harmonics in the bubble wall motion, and in the pressure field on a vibrating wall near a bubble cloud, but did not model acoustic propagation.) No such restriction to monochromatic damping physics applies to the representation of radiation loss in the Herring–Keller–Miksis family or in the Gilmore–Akulichev family of equations, which are accurate to first order in $\dot{R}/c_{\mathrm{w}}$. The former are used to calculate the volume–time histories of the bubbles in this paper. These equations assume that the bubble exists in an infinite medium, stays spherical at all times during the pulsation, and has a radius which is much smaller than the wavelength of the driving sound field. Furthermore, conditions within the bubble must be spatially uniform, no body forces (e.g. gravity) act, bulk viscous effects are negligible, and the density of the surrounding fluid is much greater than that of the internal gas. Some versions allow the gas content of the bubble to change, but limited computing resources do not allow for this in the current study.

Incorporation of thermal losses into either family of equations is computationally expensive. Hence, one option, in generating time histories to find $\mathrm{d}V/\mathrm{d}P$ for use in equation (2.10) to find ξ_{cl}, or in generating plots resembling figure 4 to obtain attenuation, would be to use a polytropic gas law in the Keller–Miksis equation. However, this route only adjusts the gas stiffness for heat flow across the bubble wall, and can never describe net thermal losses. This is because, unless the polytropic exponent varies in time, $P\,\mathrm{d}V$ is an exact differential, and each value of P defines a unique value for V. Recognizing that the results do not include net thermal losses, one could indicate to the reader the importance or otherwise of this effect by quoting, for

each time history used, the ratio of the thermal to the total dimensionless damping coefficient. However, given that this ratio is large for many of the bubble/frequency combinations, this would merely indicate that neglect of thermal damping could cause significant error. Instead, therefore, in this paper thermal damping is directly incorporated into the nonlinear model through calculation of the spatially averaged pressure in the gas. This is done by applying the perfect gas law to the spatially averaged temperature in the bubble (Nigmatulin *et al.* 1981; Prosperetti *et al.* 1988; Prosperetti & Hao 1999).

It is worth noting that this method of calculating nonlinear cross-sections via pressure–volume plots will be of value to nonlinear bubble-counting systems. Currently, in for example the analytical cross-sections used in second-harmonic or combination-frequency detectors, it is common to use, for *all* bubbles, the value of the damping coefficient calculated for resonant bubbles (Sutin *et al.* 1998). The errors introduced by this approximation, which can now be replaced, have never been quantified.

Having chosen the bubble-dynamics model, contour integration of graphs such as the middle row of figure 4 can be used to calculate the dissipation during ring-up as well as steady-state (as will be done for figure 12). However, during ring-down, in the absence of a driving pressure, the energy loss can still be calculated using the method of Clarke & Leighton (2000), as discussed at the end of § 1. We have found that a useful continuity check (to ensure, for example, that the dissipation constant is evaluated in the correct frame (Leighton 1994a)) is that the energy dissipated over the first cycle of ring-down E_1 is similar to that in any cycle of steady-state (E_s). Assuming linear exponentially decaying oscillations at the natural frequency (see figure 10), the ratio of the energy dissipated during the $(m+1)$th cycle of ring-down (E_{m+1}) to that dissipated in the previous (E_m) will be constant ($\Gamma = E_{m+1}/E_m = E_2/E_1 = E_1/E_s$). Hence, the total energy dissipated during ring-down will be

$$\sum_{m=1}^{\infty} \Gamma^m E_s = \frac{\Gamma}{1-\Gamma} E_s. \tag{2.23}$$

This completes the analysis required for the forward problem, which provides a nonlinear time-dependent model of acoustic propagation through an inhomogeneous bubble cloud. Its value might be illustrated by the fact that when stabilized gas bubbles are used *in vivo* as ultrasonic contrast agents to enhance diagnostic imaging, they are subjected to pulses of *ca.* 10 MPa in amplitude and microsecond duration. However, acoustic assessment of bubble populations of contrast agents is currently done with the assumption that the bubbles behave linearly and are driven in steady state. The signal scattered from contrast agents can be used to infer perfusion and to make quantitative measurements of volume, while assuming a constant speed of sound. The error is further compounded when one considers that, for these microbubbles at roughly 10 MPa, the time-averaged gas volume fraction (which provides the correction to the sound speed) is actually much higher than the static fraction computed using the equilibrium bubble sizes. This is a consequence of the nonlinear oscillations of the bubbles. The forward model presented in this paper would allow the errors resulting from these approaches to be assessed. Having therefore completed the forward problem, the inverse will now be discussed.

3. Inversion

The inversion method proposed is a refined version of the pioneering approach employed by Commander & McDonald (1991), now including the advantage that it incorporates a systematic approach to regularization rather than merely rendering the solution stable. The true bubble population is divided into radius bins which represent all the bubbles in a given bin by an appropriate number, $n(R_{0_j})$, all having a radius, R_{0_j}, which typifies the bin (as described in § 2). This approximation to the bubble population allows a matrix formulation to be used which relates the propagation characteristics of a plane wave propagating through a bubbly medium at discrete frequencies, ω_q, to the size distribution of the bubbles in that medium, for each volume element l of the cloud. Since matrix $\boldsymbol{K}$ is square (in a manner resembling equation (2.18)), the total number of discrete frequencies ω_q is J:

$$\boldsymbol{\alpha} = \boldsymbol{K}\boldsymbol{n}, \tag{3.1}$$

i.e.

$$
\begin{pmatrix} \alpha(\omega_1) \\ \alpha(\omega_2) \\ \alpha(\omega_3) \\ \vdots \\ \alpha(\omega_J) \end{pmatrix} =
\begin{pmatrix}
K(\omega_1, R_{0_1}) & K(\omega_1, R_{0_2}) & \cdots & K(\omega_1, R_{0_J}) \\
K(\omega_2, R_{0_1}) & K(\omega_2, R_{0_2}) & \cdots & K(\omega_2, R_{0_J}) \\
K(\omega_3, R_{0_1}) & K(\omega_3, R_{0_2}) & \cdots & K(\omega_3, R_{0_J}) \\
\vdots & \vdots & \ddots & \vdots \\
K(\omega_J, R_{0_1}) & K(\omega_J, R_{0_2}) & \cdots & K(\omega_J, R_{0_J})
\end{pmatrix}
\begin{pmatrix} n(R_{0_1}) \\ n(R_{0_2}) \\ n(R_{0_3}) \\ \vdots \\ n(R_{0_J}) \end{pmatrix}, \tag{3.2}
$$

where in this paper $\boldsymbol{\alpha}$ represents the attenuation measured at discrete frequencies (the sound speed could also be used); $\boldsymbol{K}$ is generated by the application of equation (2.18) to a range of single bubbles insonified by a set of discrete frequencies (here using the method of figure 4 to calculate the nonlinear cross-section); and $\boldsymbol{n}$ represents the bubble size distribution as discussed above (note that the potentially nonlinear attenuation $\boldsymbol{\alpha}$ in equation (3.1) is distinct from $\boldsymbol{\chi}$ in equation (2.17), which must be linear; hence, the associated kernels in the two equations will differ). In principle the inversion can be based either upon both phase speed *and* attenuation or upon either phase speed *or* attenuation. Bubbly liquids being dispersive, in this study a rigorous distinction is made between the predicted phase speed and the measured group speed, which results from the common practice of measuring transit times of acoustic pulses; particular techniques would be required to compare the two (Sasche & Pao 1978). This, with the restrictions against calculating a phase speed for dissipative bubble clouds mentioned earlier, means that here solution of equation (3.1) will be based upon attenuation only.

The formulation of § 2 has in it two features which, while available for calculating propagation through an arbitrary cloud in a forward problem, are simplified to allow inversion (considering available computing resources and the useful number of parameters which may be allowed to vary). Specifically, while the formulation allows the modelling of time-dependent propagation through an inhomogeneous bubble cloud, the inversion assumes that the cloud is homogeneous. That is to say, all the bubbles within the cloud are assumed to be driven by the same pressure amplitude. The inversion is based on the steady-state values determined from calculations such as those shown in figure 4. To illustrate why these simplifications were introduced, note that when thermal damping was incorporated into the Keller–Miksis model,

calculation of a small (10×10) matrix of bubble responses can take over 24 h on a 1 GHz Pentium III PC with 512 Mb of RAM. The neglect of amplitude variation in the driving field and temporal pulse profiles saves massively in computing time, and is justified by the eventual agreement of the forward modelling of the actual pulse with state-of-the-art predictions (figure 9). These two assumptions are not fundamental requirements, and certainly at whatever position within the bubble cloud a hydrophone is placed (here every 15 cm) the actual pressure time history as it varies through the cloud is monitored and could be used to form the elements of the K matrix. If finer spatial resolution were required, the pressure time history between hydrophones could be inferred once a first iteration of the population had been made, but currently this would represent unfeasibly greater computing costs for a minor saving in hardware.

The inverse problem of equation (3.1), i.e. estimating a bubble population from the measured attenuation, requires calculation of the matrix inverse of K:

$$n = K^{-1}\alpha. \tag{3.3}$$

However, as discussed in § 2, because the bubble scattering cross-section contains only a local maximum at the bubble resonance (figure 2), the matrix to be inverted is ill-conditioned and requires regularization for solution. This is true in both the state-of-the-art and the current techniques. To illustrate the need for regularization, consider the case when the vectors α and n in equation (3.2) are constructed such that the elements forming the leading diagonal of the matrix K describe the resonance condition (the local maximum in figure 2). With vector α running from high to low frequencies top to bottom, and n running from large to small bubbles, then the terms below the leading diagonal decrease (with the smallest value being for $K(\omega_J, R_{0_1})$, corresponding to the negligible cross-section presented by individual small bubbles to low-frequency fields). This is illustrated in the linear steady state by the behaviour close to the origin in figure 2. However, the upper right term $K(\omega_1, R_{0_J})$ is large (the large-bubble effect in figure 2) because large bubbles scatter high-frequency fields strongly. The method of regularization chosen for this paper was Tikhonov regularization (Tikhonov & Arsenin 1977) making use of the L-curve method (Hansen 1998) to determine a suitable regularization parameter. The error, e, associated with the solution, n, can be expressed as

$$e = \alpha - Kn. \tag{3.4}$$

Assuming that the functions being considered are real (i.e. only the measured attenuation or phase speed forms the input of the system), regularized solution for n is obtained by minimization of the composite cost function Ψ defined as

$$\Psi = e^{\mathrm{T}}e + \beta n^{\mathrm{T}}n, \tag{3.5}$$

where the superscript 'T' denotes a transposed matrix and the scalar β controls the amount of regularization. With some simple manipulation one obtains

$$\Psi = n^{\mathrm{T}}(K^{\mathrm{T}}K + \beta I)n - 2\alpha^{\mathrm{T}}Kn + \alpha^{\mathrm{T}}\alpha. \tag{3.6}$$

Minimization of Ψ with respect to n leads to the required value, n_{opt}:

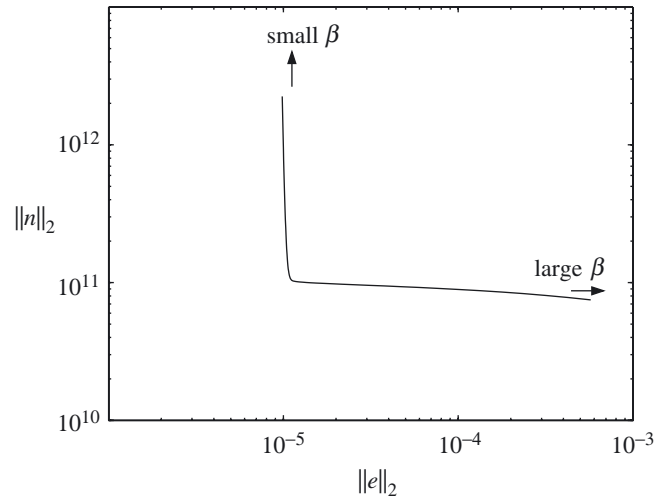$$n_{\mathrm{opt}} = (K^{\mathrm{T}}K + \beta I)^{-1}(K^{\mathrm{T}}\alpha). \tag{3.7}$$

Figure 5. Typical L-curve calculated for bubble inversion.
The optimal value of β lies at the corner of the 'L'.

One method of selecting the regularization parameter β is to plot the Euclidian norm of the regularized solution $\|\boldsymbol{n}\|_2$ against the corresponding residual norm $\|\boldsymbol{e}\|_2$ (Hansen 1998). When plotted on a log–log scale, this often forms a well-characterized 'L' shaped curve, the corner of which represents a good compromise between an over- and under-regularized solution. Figure 5 shows a typical curve calculated during an inversion of $\boldsymbol{K}$.

This technique provides a systematic method for achieving a well-regularized solution. In contrast, the method proposed by Commander & McDonald (1991) provides a value which merely renders the system stable. The corner of the 'L' shaped curve in the (y, z)-plane can be obtained by finding the maximum of the curvature, $C(y)$, given by

$$C(y) = \frac{|z''|}{(1 + z'^2)^{3/2}},\qquad(3.8)$$

where $z = \|\boldsymbol{n}\|_2$ and $y = \|\boldsymbol{e}\|_2$ and the primes refer to first and second derivatives with respect to y.

4. Experiment

A field trial employing this technique was carried out on 24 November 2001 in an attempt to estimate the bubble population in the surf zone. A feasibility study was held 12 months earlier (Leighton *et al.* 2001). The site in both cases was at the base of Hurst Spit (50° 42.48′ N, 1° 35.01′ W), which is on the south coast of England near the westerly entrance to the Solent. Attenuation under breakers with a mean wave height of *ca.* 1.0 m (i.e. smaller than during the feasibility study) was measured at a single site within *ca.* 20 m from the water line on the beach (figure 6).

While the feasibility study proved that acoustic data could be obtained (Leighton *et al.* 2001), it emphasized the extreme difficulties in making the measurement. Three different rigs were tested. The protocols ranged from inserting into the ocean a fixed scaffolding frame and then attaching transducers and sensors to it (see figure 7) to
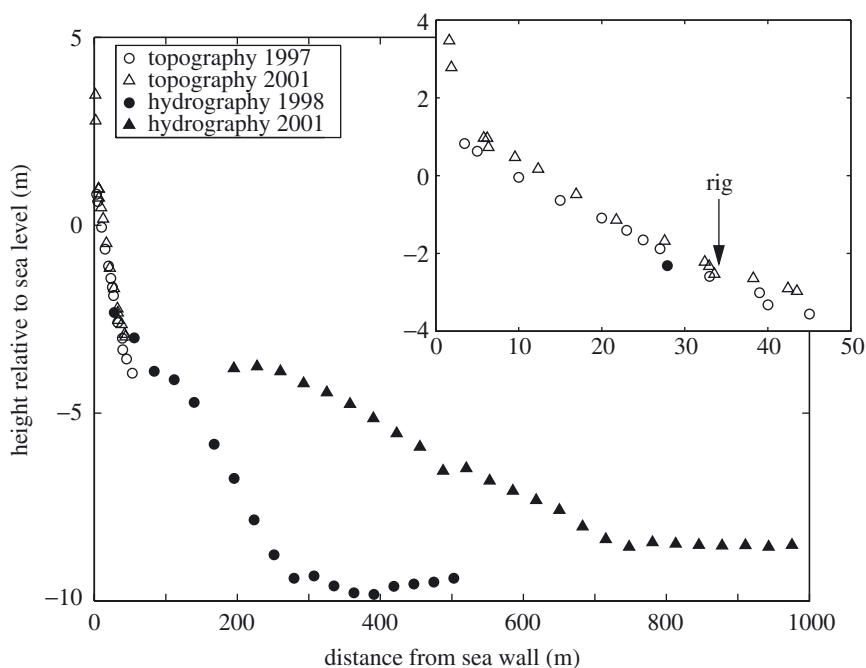
Figure 6. Topographical profile of the measurement site. The results of four surveys are shown: topographical surveys carried out on 1 September 1997 and 1 May 2001 and hydrographical surveys carried out on 1 December 1998 and 19 June 2001. Changes of up to 5 m in bed height between surveys are indicative of the dynamic nature of the site. The insert shows the topographical data in close-up and indicates the position of the measurement rig. Heights in metres corrected from Ordnance Datum Newlyn using tidal data at 16.00 GMT on 24 November 2001 to give height relative to sea level. (Data supplied by C. Eastwick & A. Bradbury.)
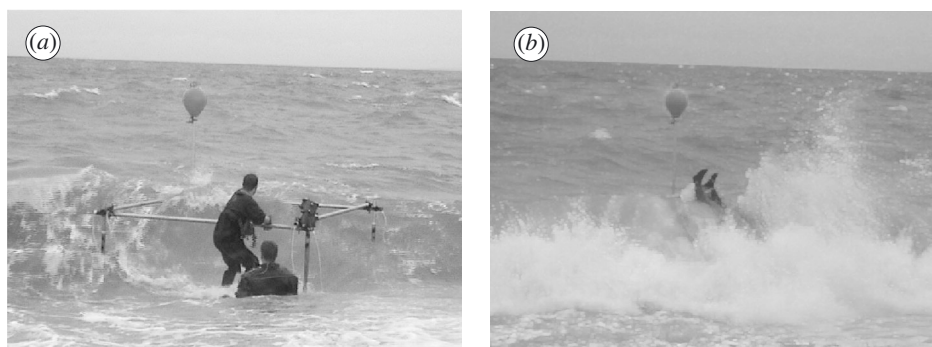
Figure 7. Two photographs, taken a fraction of a second apart in November 2000, showing (*a*) two of T.G.L.'s PhD students (S.D.M. and M. D. Simpson) attempting to bolt sensors to a scaffolding rig the team has just deployed at sea; (*b*) Simpson's feet (S.D.M. is completely buried by the wave). The waves at the measurement point are clearly more active than those further from shore in the picture (where most surf zone measurements have historically been taken). Later on during this feasibility study, the winds increased from the calm conditions shown here to speeds in excess of 50 miles per hour.
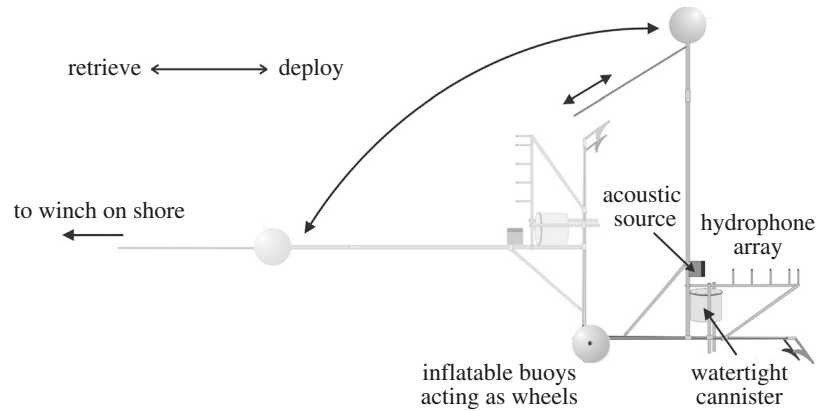
Figure 8. Schematic of rig design. The rig was wheeled down the beach in a horizontal configuration (shown in the figure as semi-transparent) and into the water to a depth of *ca.* 2 m, where it was flipped into a vertical configuration (drawn as opaque in the figure).

deploying a fully pre-assembled rig into the ocean. While at that trial the first of the options (figure 7) proved to be most successful, it was decided that, if the pre-assembled rig could be made sufficiently manoeuvrable, it would eventually prove superior. Hence the rig for the current trial was designed to be built on the beach and then deployed in a mean water depth of *ca.* 2 m. In order to maximize the depth to which the rig could be deployed against the force of the breakers, a 'flipping' design, making use of a mast *ca.* 3 m tall, was 'wheeled' out to the measurement position in a horizontal configuration. Once the measurement position was reached, the mast was flipped into a vertical configuration. Stability of the rig during measurement was ensured by scaffolding poles, which quickly embedded into the sea bed. Upon retrieval, a shore-based winch was used to apply a turning moment to the top of the mast, thereby levering the rig out of the sea bed and then allowing it to be safely dragged out of the surf. Figure 8 shows a schematic of the rig design.

Signal generation was performed using a two-channel Sony Tektronix 2010 Arbitrary Waveform Generator. Each channel was amplified by an ENI 240L power amplifier before being transmitted down the 200 m long umbilical cable. Each channel was used to drive a custom made two-element piezo-ceramic transducer with a nominal source level of 195 dB re 1 μPa at 1 m on-axis (equivalent to 7.95 kPa zero-to-peak pressure). The first element of the transducer was designed to have a frequency response that is flat to within ±2 dB from 30 kHz to 79 kHz and the second element from 80 kHz to 270 kHz. The beamwidth of each element varied from 16° at 30 kHz to 5.4° at 79 kHz and from 9.3° at 80 kHz to 3.1° at 270 kHz. This frequency range allowed the bubble population to be evaluated in the radius range 16–115 μm.

The signals generated were sequences of 10 narrowband pulses each centred about a specific frequency (corresponding to the ω_q of equation (3.2)) with a pulse length of 500 μs. This was sufficiently short that multi-path effects would not interfere with the direct pulse, but sufficiently long to confirm (through calculations such as shown in figures 3 and 4) that the use of steady-state bubble response in the inversion is warranted. Each pulse was separated from the subsequent one by 20 ms to allow any reverberation to die away. Use of narrowband pulses rather than broadband pulses improved the signal-to-noise ratio, enabling more accurate determination of signal

levels, while allowing measurement across the whole frequency range to take place in less than 250 ms. This therefore corresponds to the temporal resolution of the bubble population measured since the shorter the pulse, the closer to stationary (over the duration of the pulse) the bubble population appears, even in an environment as turbulent as the surf zone.

Signal acquisition was achieved using a line array of Bruel & Kjaer type 8103 hydrophones with a spacing of 0.15 m, the closest being 1.65 m from the source (figure 8). The pulsed-source beam pattern was modelled and mapped in an $8 \times 8 \times 5\,\mathrm{m}^3$ test tank, to ensure far-field conditions and planarity of the waveform (assumed in §2) at the hydrophones, regardless of the driving frequency and transducer element used. The output from each hydrophone was charge amplified before being transmitted down a twisted pair in the armoured 200 m umbilical cable using a 'push-pull' amplifier configuration to enable transmission of high-frequency signals and to minimize channel cross-talk and distortion. Upon receipt at the shore end, the signals were acquired at a sampling frequency of 1 MHz by a National Instruments 6110E Data Acquisition card directly onto a PC hard disk drive.

Attenuation per unit distance, $A(f)$, was calculated at each hydrophone by comparison of the amplitudes of the fast Fourier transform of the received pressure in a bubble-free laboratory environment and that measured in the surf as follows:

$$A(f) = 20 \log_{10}\left(\frac{H_2(f)}{H_1(f)}\right)\frac{1}{L_\mathrm{d}} \tag{4.1}$$

where $H_1(f)$ and $H_2(f)$ are the amplitudes of the Fourier transforms at the measurement frequency and L_d is the propagation distance, i.e. the separation of the hydrophones.

5. Results and discussion

In order to demonstrate the implications of this work, the sea-trial data have been processed using both the state-of-the-art (i.e. linear monochromatic) and the new nonlinear techniques of this paper. Figure 9 shows the two estimated bubble size distributions, each colour representing a measurement at a different time: the dashed line for a given colour represents inversion using the linear monochromatic technique, and the solid line represents inversion of the same acoustic data using the nonlinear technique.

Comparisons of measured data (as shown in figure 9) with the dynamic modelling of figure 1 are as yet at an early stage. However, it is heartening to note the qualitative similarities, for example, the position of the peak of the distribution in the radius domain. While the assumption of monochromatic linearity inherent in the state-of-the-art technique has been violated by the measurement (as illustrated by figure 10), nevertheless, the bubble populations inferred by the state-of-the-art method are very close to those estimated using the new technique at the 10 kPa-or-less driving pressures used here.

The effects of changing the driving amplitude are illuminating. A single bubble population, calculated using the linear kernel (black curve), was used as the basis for the calculation of attenuation (the forward problem, described above). This linearly calculated attenuation was then compared with the attenuations calculated using the new, nonlinear kernel, making the assumption that the driving pressures were 100 Pa,
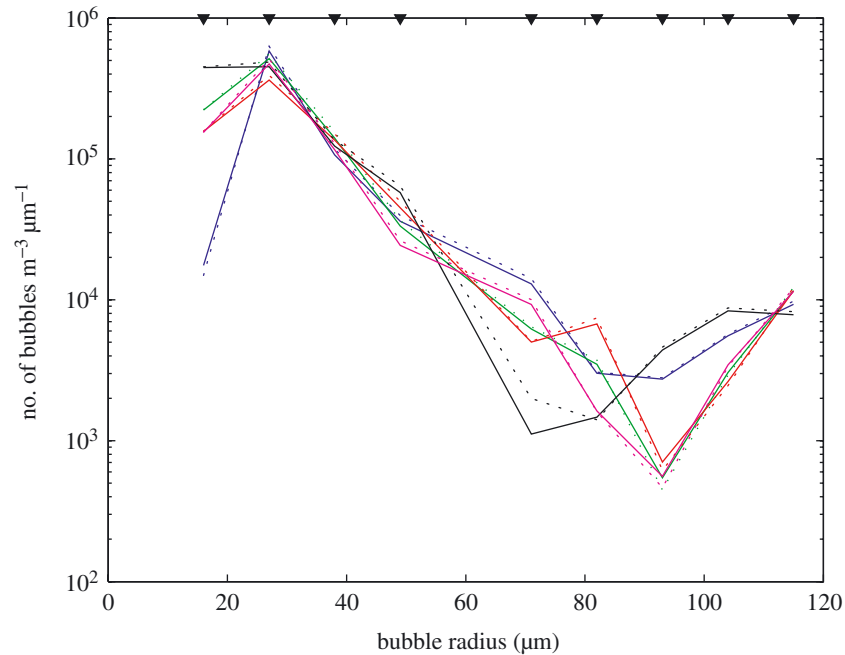
Figure 9. Histogram of the number of bubbles per cubic metre of sea water, per micrometre increment in radius, as a function of bubble radius, taken from 15.20 to 16.00 GMT on 24 November 2001. The average wind speed during these measurements was 4 m s^{-1} from a southwesterly direction, the water temperature was $8\,^\circ\text{C}$ and the air temperature was $11\,^\circ\text{C}$. The electrical conductivity was 49.5 mS cm^{-1}, the pH was 8.07 and the salinity was 34.1‰. Each separate colour indicates measurement at a different time. For a given colour, the dotted curves show the bubble population obtained by applying the state-of-the-art inversion to the acoustic data. The solid curve of the same colour shows the population obtained when the same acoustic data are inverted using the new theory. Hence the solid curves present, for the first time, bubble populations obtained by an inversion which does not assume linear monochromatic conditions. The void fractions are around 5×10^{-6}. The arrowheads at the top of the figure are aligned with the bubble radii which would be resonant with the discrete centre driving frequencies chosen (data corresponding to $R_0 = 60\,\mu\text{m}$ were not processed owing to sea-trial difficulties).

20 kPa and 50 kPa. Linear mathematics would predict that the attenuation is independent of the driving amplitude. Figure 11 shows that the low-amplitude nonlinear solution is indistinguishable from the linear solution (such convergence can only ever be a partial check of correctness, since any errors in the nonlinear terms will also be small under such conditions). However, there is increasing deviation from the linear prediction as the driving amplitude increases. These higher amplitudes are achievable by many commercial and military ocean acoustic systems (Urick 1983). It is at these higher driving pressures that the calculation of the nonlinear effects described in this paper becomes increasingly important. If, for example, higher driving pressures tend to produce lower-than-expected attenuations, the bubble population inferred by the high-amplitude state-of-the-art system may be an underestimate.

As attempts are made to explore populations with higher void fractions and consequently attenuations, the amplitude of the insonifying field will need to increase, and so too will the errors in the state-of-the-art methods. Such fields might be used in
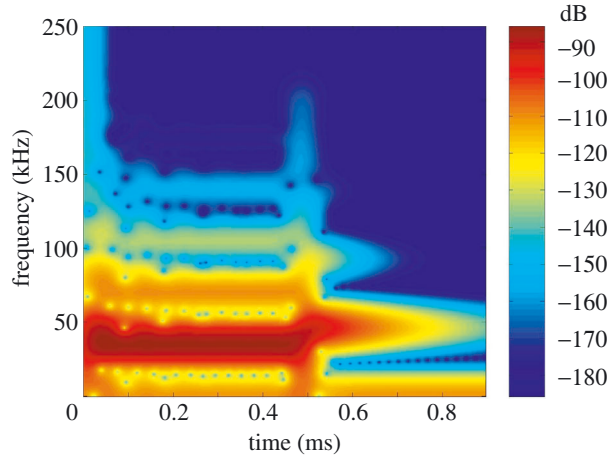
Figure 10. A spectrogram plot of power spectral density (arbitrary reference) calculated for the radius time history of a 106 μm radius air bubble being driven at 30 987 Hz and 7.95 kPa. Significant energy is present at higher harmonics, indicating a departure from the monochromatic, linear regime. The drive frequency, which equals the bubble fundamental during steady-state (200–500 μs), is lower than the bubble pulsation natural frequency, which can be seen both during ring-down (corresponding to times greater than 500 μs) and the transient period.
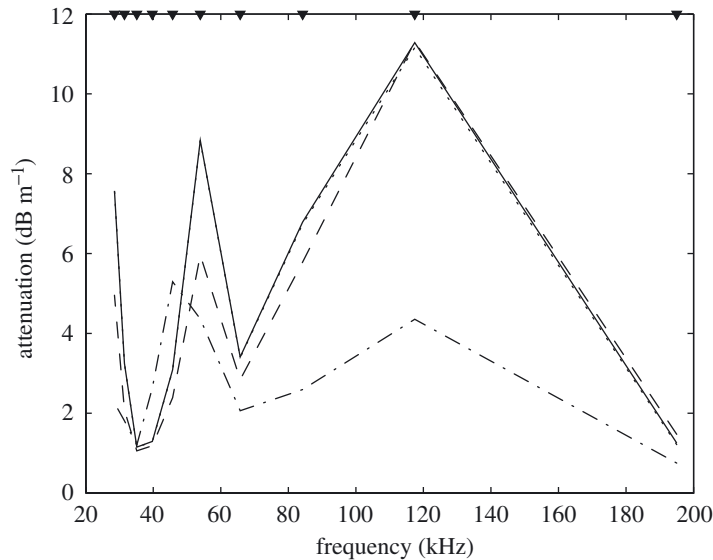
Figure 11. Steady-state attenuation calculated assuming the bubble population estimated in the black dotted curve of figure 9. The calculation is performed using the linear formulation of Commander & Prosperetti (equation (2.14); solid line) as well as the new nonlinear formulation assuming different driving pressures: 100 Pa (dotted line), 20 kPa (dashed line) and 50 kPa (dash-dotted line). The 100 Pa nonlinear solution (dotted line) almost overlies the linear solution (solid line). Note that the lines do not imply data across a continuum of frequencies: the calculation is performed at the 10 specific pump frequencies used in the experiment (indicated by arrowheads at the top of the figure). Since these frequencies were chosen to give even point spacing in radii for figure 9, the spacing of points is sparse at high frequencies.

industry, biomedicine or the oceans, including waves, wakes and the bubble curtains of cetaceans (Leighton *et al.* 2004*b*). It should be noted that, on the day of the trial, conditions in the surf zone were milder than expected. Hence, denser populations than seen in figure 9 might be observed (using a nonlinear technique, Phelps *et al.* (1997) measured bubble populations in the surf zone peaking at nearly 10^7 m^{-3} per micrometre radius increment).

As discussed in § 2, the technique can incorporate time-dependent, as well as nonlinear, bubble-cloud behaviour. As a demonstration, figure 12 shows the time-dependent response of the same bubble cloud as was used to provide the data in figure 11. The cloud is subjected to a semi-infinite pulse, and the loss is calculated by contour-integration of the P–V loops from time zero up to the number of cycles of the pump field indicated in the legend. Dividing this integration by the number of cycles over which it was performed allows calculation of the average attenuation *per cycle*. As expected, as time increases (20 or 50 cycles), this tends to the steady-state solution of figure 11, with the amplitude dependence already discussed. The attenuation per cycle is almost independent of pulse amplitude for the shortest integrations (1–2 cycles). At 50 kPa driving pressures, the greatest attenuation per cycle is seen for the five-cycle integration at most frequencies. These observations are of course preliminary, referring specifically to the cloud used and the frequencies at which the calculations are performed (show by arrows above the graphs). Production of figure 12 required calculation of time-dependent kernels K_{qj} and hence would make time-dependent inversions possible.

Figures 11 and 12 also suggest a further advance in bubble counting, specifically by performing the inversion based upon pulses which are closely spaced in time but have different amplitudes and/or temporal profile. From analysis of the different estimated size distributions it would be possible to infer a confidence level upon the estimate of the bubble population. Furthermore, inversion of both high- and low-amplitude data by the state-of-the-art method should incorrectly indicate two different bubble populations. However, inversion of both by the new technique (which for the low-amplitude pulses is equivalent to the state-of-the-art method) would for the first time provide measurement of an oceanic cloud by two techniques *which sample it identically, using the same hardware* (not achieved previously—see § 1). This would, for example, allow a single-frequency source to obtain bubble population data over an octave or more (Leighton *et al.* 2004*a*). This advantage can be extended to other techniques which currently assume linear bubble oscillations (e.g. the resonator method; Medwin & Clay 1998; Farmer *et al.* 1998). In the special case of high void fractions this dual-amplitude technique presents another intriguing possibility: because the attenuation in the nonlinear regime will vary with driving pressure, it may be possible to infer the bubble population from the difference in attenuation measured for two high amplitude pulses. This has the potential advantage that bubble–bubble interactions (the main obstacle to successful high void fraction inversions) would, to first order, be accounted for in this method.

Recent studies (Ye & Ding 1995; Feuillade 1996; Henyey 1999) have considered the effect of bubble–bubble interactions on acoustic propagation in bubbly environments. Kargl (2002) proposes a corrected form of Commander & Prosperetti's linear wavenumber (equation (2.14)) with the radiation damping re-expressed in terms of the effective damping seen by the bubble. While this solution assumes linearity, it is still useful for giving an indication of the likely effect of bubble interactions upon surf

zone measurements. Figure 13 shows the linearly predicted attenuation with and without the inclusion of bubble–bubble interactions for bubble populations based on the size distribution of figure 9, but scaled to give void fractions (VF) ranging between 5×10^{-6} and 10^{-3}. This population was then used to solve the forward problem employing both equation (2.14) and Kargl's expression. Taking, for example, a signal at 39.7 kHz in a void fraction of 10^{-4}, the $78.4\,\mathrm{dB\,m^{-1}}$ attenuation predicted by Kargl's method would suggest a requirement for amplitudes sufficient to excite bubble nonlinearity. Given, however, that even with such strong dissipation this is only $0.2\,\mathrm{dB\,m^{-1}}$ less than that predicted when bubble–bubble interactions are neglected, comparison between figures 11 and 13 suggests that the errors generated by neglecting nonlinearity might exceed those produced by neglecting bubble–bubble interactions over that part of the propagation path where the driving amplitude is sufficiently high. Kargl's equation presents the possibility of incorporating bubble–bubble interactions into an inverse method. An iterative scheme could be developed whereby estimated bubble numbers are used to modify the radiation damping term and hence predict a new set of estimates. This process could be repeated until a stable solution is achieved (experience with the forward solution indicates that a small number of iterations would be required). However, this technique would only be beneficial with higher void fractions than those measured in this study.

It should not, however, be thought that the inclusion of bubble nonlinearity is an obligation made necessary only when void fractions or propagation paths are very great, making high insonifying amplitudes necessary. Rather, the ability to generate, describe and invert bubble nonlinearity in propagation provides an additional diagnostic tool even at low void fractions. The time-varying, nonlinear and amplitude-dependent characteristics which the bubbles impart to acoustic attenuation, sound speed and, particularly, scattering, could be exploited to distinguish from bubbles those objects which do not (Leighton 2004). If, for example, the incident time-series contains two consecutive pulses, the second having reverse polarity with respect to the first, then addition of the scatter from these two pulses will enhance the echoes from the nonlinear scatterers (bubbles) and suppress those from the linear scatterers (e.g. for use when enhancing the signal from biomedical ultrasonic contrast agents). However, subtraction of the scatter from these two pulses will enhance the echoes from the linear scatterers and suppress those from the nonlinear ones (the bubbles) (Leighton 2004). This would be important for the detection of, for example, solid targets (such as mines) in the surf zone.

The technique outlined in this paper still maintains certain assumptions, including linearity of the acoustic propagation and the limitations on void fraction discussed earlier. While with some features (such as the planarity of the incident wave) it is possible to control the experiment to see that they match the assumptions of theory, for other features this is not possible. They are a necessary part of the environment being measured. For example, anomalous values of bubble damping have been attributed to the existence of both bubble shape oscillations (Longuet-Higgins 1992) and reverberation (Leighton *et al.* 2002). It is likely that no bubble acoustics data have ever been gathered in a perfectly free field. It is interesting to note that, in comparing their theory with data taken in reverberant (e.g. standing wave) conditions, Commander & Prosperetti found that the poorest agreement occurred when the effects of bubble resonances were strong. This is in agreement with the conditions for maximum error in free-field theory predicted by Leighton *et al.* (2002).
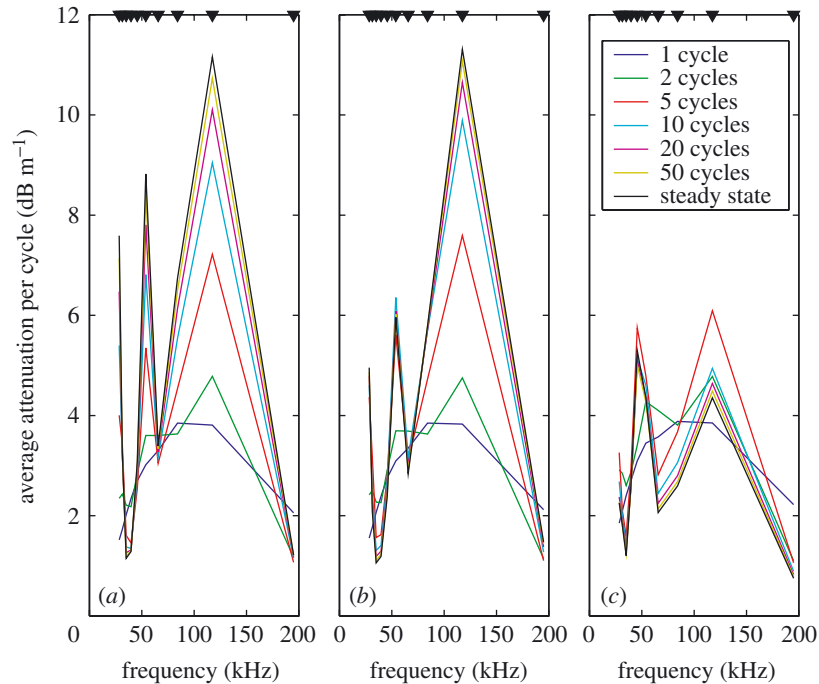
Figure 12. Averaged attenuation per cycle calculated for different pulse lengths and amplitudes. Each graph shows the effect of increasing pulse length for a fixed driving amplitude. Note that as the pulse length increases the attenuation tends toward the steady-state solution of figure 11 (black line). The driving amplitudes used are (*a*) 100 Pa, (*b*) 20 kPa and (*c*) 50 kPa. As with figure 11, the data are plotted at 10 discrete frequencies corresponding to a linear spacing of bubble radii, and hence there are few data points at high frequency.

6. Conclusion

This paper describes a technique for predicting attenuation during acoustic propagation through an inhomogeneous bubble cloud. The theoretical framework is generic, in that any bubble dynamics model (even, for example, bubbles in sediment or multiply interacting bubbles) may be incorporated to predict propagation. The model chosen for particular study incorporates time dependency and nonlinearity into the response of bubbles, and includes the precise temporal nature of the sound field. As a result, when this system is used to invert the propagation characteristics to estimate the bubble population, the assumptions of monochromaticity, steady state and linearity present in the state-of-the-art inversion are not in principle required. However, to comply with computing resource limitations and to place sensible limits on the inversion, assumptions of cloud homogeneity and bubble steady state are used when this method is tested in a field trial. Preliminary calculations for higher amplitudes than those used in the trial suggest that the state-of-the-art methods may tend to miscalculate the attenuation predicted in the forward problem, and the bubble population estimated when it is used in the inverse problem, as the driving pressure increases. Such errors may be greater than those introduced by neglecting bubble–bubble interactions. Time-dependent nonlinear attenuations have been mod-
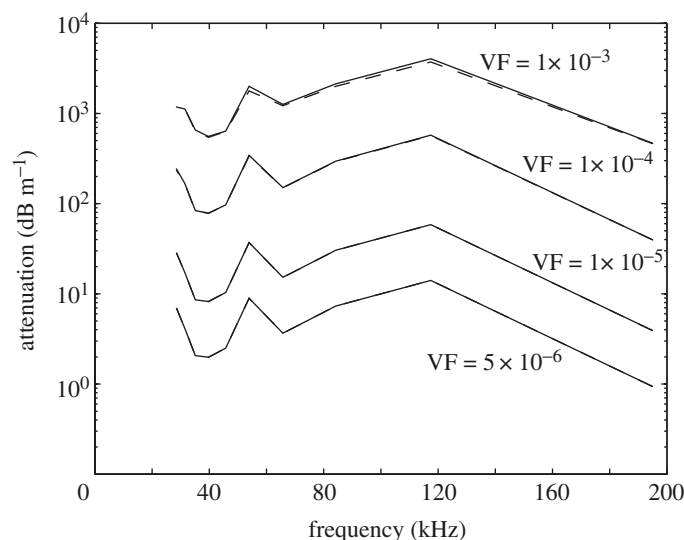
Figure 13. Attenuation predicted using both standard linear theory (solid lines) and Kargl's theory that accounts for bubble–bubble interactions (dashed lines). A typical bubble population from figure 9 is scaled up to void fractions of 10^{-5}, 10^{-4} and 10^{-3}, and compared with the attenuation caused by the original void fraction (5×10^{-6}).

elled. Further advances are suggested through the application of signals containing consecutive pulses of varying amplitude and profile.

References

Caflisch, R. E., Miksis, M. J., Papanicolaou, G. C. & Ting, L. 1985 Effective equations for wave propagation in bubbly liquids. *J. Fluid Mech.* **153**, 259–273.

Clarke, J. W. L. & Leighton, T. G. 2000 A method for estimating time-dependent acoustic cross-sections of bubbles and bubble clouds prior to the steady state. *J. Acoust. Soc. Am.* **107**, 1922–1929.

Commander, K. W. & McDonald, R. J. 1991 Finite-element solution of the inverse problem in bubble swarm acoustics. *J. Acoust. Soc. Am.* **89**, 592–597.

Commander, K. W. & Moritz, E. 1989 Off-resonance contributions to acoustical bubble spectra. *J. Acoust. Soc. Am.* **85**, 2665–2669.

Commander, K. W. & Prosperetti, A. 1989 Linear pressure waves in bubbly liquids: comparison between theory and experiments. *J. Acoust. Soc. Am.* **85**, 732–746.

Dahl, P. H. 2001 Bubble clouds and their transport within the surf zone as measured with a distributed array of upward-looking sonars. *J. Acoust. Soc. Am.* **109**, 133–142.

Deane, G. B. 1997 Sound generation and air entrainment by breaking waves in the surf zone. *J. Acoust. Soc. Am.* **102**, 2671–2689.

Deane, G. B. & Stokes, M. D. 2002 Scale dependence of bubble creation mechanisms in breaking waves. *Nature* **418**, 839–844.

Didenkulov, I. N., Muyakshin, S. I. & Selivanonsky, D. A. 2001 Bubble counting in the subsurface ocean layer. In *Acoustical oceanography* (ed. T. G. Leighton, G. J. Heald, H. Griffiths & G. Griffiths). Proceedings of the Institute of Acoustics, vol. 23, part 2, pp. 220–226. Bath University Press.

Dumbrell, H. A. 1997 Comparison of excess attenuation and backscatter measurements of ship wakes. In *Proc. 4th Int. Conf. Natural Physical Processes Associated with Sea Surface Sound* (ed. T. G. Leighton), pp. 171–178. University of Southampton.

Duraiswami, R., Sankar, P. & Chahine, G. L. 1998 Bubble counting using an inverse acoustic scattering method. *J. Acoust. Soc. Am.* **104**, 2699–2717.

Eller, A. I. 1970 Damping constants of pulsating bubbles. *J. Acoust. Soc. Am.* **47**, 1469–1470.

Farmer, D. M. 2001 Acoustic remote sensing near the air–sea interface. In *Acoustical oceanography* (ed. T. G. Leighton, G. J. Heald, H. Griffiths & G. Griffiths). Proceedings of the Institute of Acoustics, vol. 23, part 2, pp. 128–134. Bath University Press.

Farmer, D. M. & Vagle, S. 1989 Waveguide propagation of ambient sound in the ocean-surface bubble layer. *J. Acoust. Soc. Am.* **86**, 1897–1908.

Farmer, D. M., McNeil, C. L. & Johnson, B. D. 1993 Evidence for the importance of bubbles in increasing air–sea gas flux. *Nature* **361**, 620–623.

Farmer, D. M., Vagle, S. & Booth, A. D. 1998 A free-flooding acoustical resonator for measurement of bubble size distributions. *J. Atmos. Ocean. Technol.* **15**, 1132–1146.

Farmer, D. M., Deane, G. B. & Vagle, S. 2001 The influence of bubble clouds on acoustic propagation in the surf zone. *IEEE J. Oceanic Engng* **26**, 113–124.

Feuillade, C. 1996 The attenuation and dispersion of sound in water containing multiply interacting air bubbles. *J. Acoust. Soc. Am.* **99**, 3412–3430.

Geissler, P. & Jahne, B. 1997 Laboratory and inshore measurements of bubble size distributions. In *Proc. 4th Int. Conf. Natural Physical Processes Associated with Sea Surface Sound* (ed. T. G. Leighton), pp. 147–154. University of Southampton.

Hansen, P. C. 1998 *Rank-deficient and discrete ill-posed problems: numerical aspects of linear inversion.* Philadelphia, PA: SIAM.

Henyey, F. S. 1999 Corrections to Foldy's effective medium theory for propagation in bubble clouds and other collections of small scatterers. *J. Acoust. Soc. Am.* **105**, 2149–2154.

Kargl, S. G. 2002 Effective medium approach to linear acoustics in bubbly liquids. *J. Acoust. Soc. Am.* **111**, 168–173.

Kolovayev, P. A. 1976 Investigation of the concentration and statistical size distribution of wind produced bubbles in the near-surface ocean layer. *Oceanology* **15**, 659–661.

Kumar, S. & Brennen, C. E. 1991 Nonlinear effects in the dynamics of clouds of bubbles. *J. Acoust. Soc. Am.* **89**, 707–714.

Kumar, S. & Brennen, C. E. 1993 Some nonlinear interactive effects in bubbly clouds. *J. Fluid Mech.* **253**, 565–591.

Leighton, T. G. 1994*a The acoustic bubble*, §§ 2.1.3, 3.2.1, 3.3.1(b), 4.2.1, 4.2.2. Academic Press.

Leighton, T. G. 1994*b* Acoustic bubble detection. I. The detection of stable gas bodies. *Environ. Engng* **7**, 9–16.

Leighton, T. G. 2001 Inaugural Medwin award address. Surf zone bubble spectrometry: the role of the acoustic cross-section. *J. Acoust. Soc. Am.* **110**, 2694.

Leighton, T. G. 2004 Nonlinear bubble dynamics and the effects on propagation through near-surface bubble layers. In *High-frequency ocean acoustics* (ed. M. B. Porter, M. Siderius & W. Kuperman). Melville, NY: American Institute of Physics. (In the press.)

Leighton, T. G. & Walton, A. J. 1987 An experimental study of the sound emitted from gas bubbles in a liquid. *Eur. J. Phys.* **8**, 98–104.

Leighton, T. G., Phelps, A. D. & Ramble, D. G. 1996 Acoustic bubble sizing: from laboratory to the surf zone trials. *Acoust. Bull.* **21**, 5–12.

Leighton, T. G. (and 10 others) 2001 The Hurst Spit experiment: the characterization of bubbles in the surf zone using multiple acoustic techniques. In *Acoustical oceanography* (ed. T. G. Leighton, G. J. Heald, H. Griffiths & G. Griffiths), Proceedings of the Institute of Acoustics, vol 23, part 2, pp. 227–234. Bath University Press.

Leighton, T. G., White, P. R., Morfey, C. L., Clarke, J. W. L., Heald, G. J., Dumbrell, H. A. & Holland, K. R. 2002 The effect of reverberation on the damping of bubbles. *J. Acoust. Soc. Am.* **112**, 1366–1376.

Leighton, T. G., Dumbrell, H. A. & Heald, G. J. 2004*a* The possibility and exploitation of nonlinear effects in the near-surface oceanic bubble layer. In *Proc. 7th European Conf. on Underwater Acoustics, ECUA 2004, Delft, The Netherlands.* (In the press.)

Leighton, T. G., Richards, S. D. & White, P. R. 2004*b* Trapped within a 'wall of sound': a possible mechanism for the bubble nets of humpback whales. *Acoust. Bull.* **29**, 24–29.

Longuet-Higgins, M. S. 1992 Nonlinear damping of bubble oscillations by resonant interaction. *J. Acoust. Soc. Am.* **91**, 1414–1422.

Medwin, H. 1977 *In situ* acoustic measurements of microbubbles at sea. *J. Geophys. Res.* **82**, 971–976.

Medwin, H. & Beaky, M. W. 1989 Bubble sources of the Knudsen sea noise spectra. *J. Acoust. Soc. Am.* **86**, 1124–1130.

Medwin, H. & Clay, C. S. 1998 *Fundamentals of acoustical oceanography.* Academic.

Meers, S. D., Leighton, T. G., Clarke, J. W. L., Heald, G. J., Dumbrell, H. A. & White, P. R. 2001 The importance of bubble ring-up and pulse length in estimating the bubble distribution from propagation measurements. In *Acoustical oceanography* (ed. T. G. Leighton, G. J. Heald, H. Griffiths & G. Griffiths). Proceedings of the Instute of Acoustics, vol. 23, part 2, pp. 235–241. Bath University Press.

Melville, W. K., Terril, E. & Veron, F. 1997 Bubbles and turbulence under breaking waves. In *Proc. 4th Int. Conf. Natural Physical Processes Associated with Sea Surface Sound* (ed. T. G. Leighton), pp. 135–146. University of Southampton.

Minnaert, M. 1933 On musical air-bubbles and sounds of running water. *Phil. Mag.* **16**, 235–248.

Nigmatulin, R. I., Khabeev, N. S. & Nagiev, F. B. 1981 Dynamics, heat and mass transfer of vapour-gas bubbles in a liquid. *Int. J. Heat Mass Transfer* **24**, 1033–1044.

Nyborg, W. L. (ed.) 2002 ANSI Technical Report S1.24 TR-2002. New York: Acoustical Society of America.

Phelps, A. D. & Leighton, T. G. 1998 Oceanic bubble population measurements using a buoy-deployed combination frequency technique. *IEEE J. Oceanic Engng* **23**, 400–410.

Phelps, A. D., Ramble, D. G. & Leighton, T. G. 1997 The use of a combination frequency technique to measure the surf zone bubble population. *J. Acoust. Soc. Am.* **101**, 1981–1989.

Prosperetti, A. 1974 Nonlinear oscillations of gas bubbles in liquids: steady state solutions. *J. Acoust. Soc. Am.* **56**, 878–885.

Prosperetti, A. & Hao, Y. 1999 Modelling of spherical gas bubble oscillations and sonoluminescence. *Phil. Trans. R. Soc. Lond.* A **357**, 203–223.

Prosperetti, A., Crum, L. A. & Commander, K. W. 1988 Nonlinear bubble dynamics. *J. Acoust. Soc. Am.* **83**, 502–514.

Pumphrey, H. C., Crum, L. A. & Bjorno, L. 1989 Underwater sound produced by individual drop impacts and rainfall. *J. Acoust. Soc. Am.* **85**, 1518–1526.

Sasche, W. & Pao, Y.-H. 1978 On the determination of phase and group velocities of dispersive waves in solids. *J. Appl. Phys.* **49**, 4320–4327.

Stokes, M. D. & Deane, G. B. 1999 A new optical instrument for the study of bubbles at high void fractions within breaking waves. *IEEE J. Oceanic Engng* **24**, 300–311.

Su, M.-Y., Todoroff, D. & Cartmill, J. 1994 Laboratory comparisons of acoustic and optical sensors for microbubble measurement. *J. Atmos. Ocean. Technol.* **11**, 170–181.

Sutin, A. M., Yoon, S. W., Kim, E. J. & Didenkulov, I. N. 1998 Nonlinear acoustic method for bubble density measurements in water. *J. Acoust. Soc. Am.* **103**, 2377–2384.

Svendsen, I. A., Madsen, P. A. & Hansen, J. B. 1978 Wave characteristics in the surf zone. In *Proc. 16th Coastal Engineering Conf.*, pp. 520–539. New York: Academic Society of Civil Engineers.

Terrill, E. J. & Melville, W. K. 1998 A broadband acoustic technique for measuring bubble size distribution: laboratory and shallow water measurements. *J. Atmos. Ocean. Technol.* **17**, 220–239.

Terrill, E. J., Lada, G. & Melville, W. K. 2001 Surf zone bubble populations. In *Acoustical oceanography* (ed. T. G. Leighton, G. J. Heald, H. Griffiths & G. Griffiths). Proceedings of the Institute of Acoustics, vol. 23, part 2, pp. 212–219. Bath University Press.

Thorpe, S. A. 1982 On the clouds of bubbles formed by breaking wind-waves in deep water, and their role in air–sea gas transfer. *Proc. R. Soc. Lond.* A **304**, 155–210.

Thorpe, S. A., Bowyer, P. & Woolf, D. K. 1992 Some factors affecting the size distributions of oceanic bubbles. *J. Phys. Oceanogr.* **22**, 382–389.

Tikhonov, A. N. & Arsenin, V. Y. 1977 *Solution of ill-posed problems*. Wiley.

Updegraff, G. E. & Anderson, V. C. 1989 *In situ* acoustic signature of low sea-state microbreaking. *J. Acoust. Soc. Am.* **85**, 1–146.

Urick, R. J. 1983 *Principles of underwater sound*. McGraw-Hill.

van Wijngaarden, L. 1968 On the equations of motion for mixtures of liquid and gas bubbles. *J. Fluid Mech.* **33**, 465–474.

Ye, Z. & Ding, L. 1995 Acoustic dispersion and attenuation relations in bubbly mixture. *J. Acoust. Soc. Am.* **98**, 1629–1636.